RESEARCH ARTICLE

Key Points:
- A new Artificial Neural Network based global 2-D Ionospheric Model (ANNIM) is developed to predict the ionospheric N_mF_2 and h_mF_2 variations
- ANNIM has well captured the spatial and temporal variations of N_mF_2 and h_mF_2 and reproduced the EIA, annual anomaly, MSNA, WSA, etc.
- Current ANNIM predictions are as good as IRI-2016 model with a slight improvement and can be further improved to develop a 3-D model

An Artificial Neural Network-Based Ionospheric Model to Predict N_mF_2 and h_mF_2 Using Long-Term Data Set of FORMOSAT-3/COSMIC Radio Occultation Observations: Preliminary Results

V. Sai Gowtam[1] [iD] and S. Tulasi Ram[1] [iD]

[1]Indian Institute of Geomagnetism, Navi Mumbai, India

Abstract Artificial Neural Networks (ANNs) are known to be capable of solving linear as well as highly nonlinear problems. Using the long-term and high-quality data set of Formosa Satellite-3/Constellation Observing System for Meteorology, Ionosphere, and Climate (FORMOSAT-3/COSMIC, in short F3/C) from 2006 to 2015, an ANN-based two-dimensional (2-D) Ionospheric Model (ANNIM) is developed to predict the ionospheric peak parameters, such as N_mF_2 and h_mF_2. In this pilot study, the ANNIM results are compared with the original F3/C data, GRACE (Gravity Recovery and Climate Experiment) observations as well as International Reference Ionosphere (IRI)-2016 model to assess the learning efficiency of the neural networks used in the model. The ANNIM could well predict the N_mF_2 (h_mF_2) values with RMS errors of 1.87×10^5 el/cm^3 (27.9 km) with respect to actual F3/C; and 2.98×10^5 el/cm^3 (40.18 km) with respect to independent GRACE data. Further, the ANNIM predictions found to be as good as IRI-2016 model with a slightly smaller RMS error when compared to independent GRACE data. The ANNIM has successfully reproduced the local time, latitude, longitude, and seasonal variations with errors ranging ~15–25% for N_mF_2 and 10–15% for h_mF_2 compared to actual F3/C data, except the postsunset enhancement in h_mF_2. Further, the ANNIM has also captured the global-scale ionospheric phenomena such as ionospheric annual anomaly, Weddell Sea Anomaly, and the midlatitude summer nighttime anomaly. Compared to IRI-2016 model, the ANNIM is found to have better represented the fine longitudinal structures and the midlatitude summer nighttime enhancements in both the hemispheres.

1. Introduction

A comprehensive understanding of the ionospheric structure and dynamics is essential for the near-real-time forecast and long-term prediction of the ionospheric parameters to serve the satellite-based communication and navigation needs. Theoretical or physics-based models are developed by understanding the physical, chemical, and transport processes that control the variability of coupled thermosphere-ionosphere system (Schunk, 1996). By systematically understanding the effects of background ionospheric conditions such as electric fields, neutral winds, solar flux, and geomagnetic conditions, the physics-based models can predict the temporal and spatial variability of ionospheric parameters. The Time-Dependent Ionospheric Model (Schunk et al., 1976, 1975; Schunk & Walker, 1973), thermosphere-ionosphere-electrodynamics general circulation model (Richmond et al., 1992; Roble et al., 1988), thermosphere-ionosphere-mesosphere electrodynamics general circulation model (Roble & Ridley, 1994), parameterized ionospheric model (Daniell et al., 1995), coupled thermospheric ionospheric model (Fuller-Rowell et al., 1996), Shuffled University plasmaspheric ionospheric model (Bailey & Balan, 1996; Bailey et al., 1997), and SAMI2 is Another Model of the Ionosphere (SAMI2) (Huba et al., 2000) are some of the physics-based models. On the other hand, the International Reference Ionosphere (IRI) (Bilitza, 2001) and NeQuick (Hochegger et al., 2000; Nava et al., 2006; Radicella & Leitinger, 2001) are the empirical models, developed by assimilating the several ground and spaceborne observations globally. Several methods are being incorporated to model the local time, latitude, longitude, and solar cycle variability of the ionosphere by the scientific community across the world. Each model has its own advantages and disadvantages; however, the accurate prediction of the ionospheric conditions is still a challenging task because of its complex variability due to several controlling factors (Anderson et al., 1998; Shunk & Sojka, 1996).

The Artificial Neural Networks (ANNs) and machine learning can solve more complex problems by systematic learning mechanisms. Numerous studies on prediction of ionospheric peak electron density (N_mF_2), total

electron content (TEC), sunspot number, interplanetary conditions using ANNs can be found in the literature (Athieno et al., 2017; Huang & Yuan, 2014; Kumluca et al., 1999; Lamming & Cander, 1999; Macpherson et al., 1995; Poole & Poole, 2002; Watthanasangmechai et al., 2012; Williscroft & Poole, 1996; Wintoft, 2000; Xenos, 2002; Zhao et al., 2014). Earlier attempts to forecast the N_mF_2 and TEC using neural networks were based on daily and monthly time scales. Altinay et al. (1997) implemented multilayer perceptron-type neural networks to forecast the ionospheric critical frequency (f_oF_2). Ma et al. (2005) used residual minimization training neural network in ionospheric tomography to reconstruct the local ionospheric electron density distribution. By implementing the genetic algorithm based neural networks, Zhou et al. (2013) tried to predict the f_oF_2. The aforementioned studies on ionospheric prediction are mostly confined to over a given location. Oyeyemi and Poole (2004) and Oyeyemi et al. (2005) developed a global f_oF_2 model and discussed the forecasting capabilities of the neural network-based models. Recently, neural networks are being used in the magnetospheric studies as well (Dmitriev & Suvorova, 2000; Shin et al., 2016; Zhelavskaya et al., 2016). All the above studies show the potentiality of the neural networks and its application in the fields of ionosphere and magnetosphere. In the view of the capabilities of the ANNs, the main objective of the present study is to develop an Artificial Neural Network based Ionospheric Model (ANNIM) to predict the ionospheric F_2 region peak parameters such as N_mF_2 and h_mF_2, globally, using the long-term radio occultation (RO) data set of Formosa Satellite-3/Constellation Observing System for Meteorology, Ionosphere, and Climate (FORMOSAT-3/COSMIC (F3/C)).

2. Data and Methodology

With a constellation of six microsatellites around 800 km circular orbits, the F3/C radio occultation experiment provides the height profiles of atmospheric parameters and ionospheric electron density. With nearly 2,000 profiles per day, F3/C provided unprecedented coverage of ionospheric vertical electron density profile observations with a nearly uniform spatial distribution over the globe. Further, the retrieved electron density profiles from F3/C are found in good agreement with ground-based incoherent scatter radar and ionosonde observations (Lei et al., 2007; Schreiner et al., 2007). In the present study, we have used the ionospheric peak electron density (N_mF_2) and the peak height of F_2 layer (h_mF_2) derived from the F3/C electron density profiles during 2006–2015 (http://cdaac-www.cosmic.ucar.edu). All the electron density profiles were initially processed for quality control, and profiles with a mean standard deviation greater than 1.5 and/or F_2 layer peak height (h_mF_2) greater than 500 km were removed from the analysis using the method suggested by Yang et al. (2009), Potula et al. (2011), and Uma et al. (2016). The daily averaged $F_{10.7}$ solar flux and 3-hourly Kp index data are obtained from the Space Physics Data Facility of NASA, USA (https://omniweb.gsfc.nasa.gov). Figure 1a shows the daily averaged $F_{10.7}$ solar flux for the entire data range, starting from 2006 to 2015. Figure 1b shows the number of electron density profiles from F3/C in each month indicating the quantum of the data that used in the present study. The blue bars indicate the total number of F3/C profiles, and the green bars indicate the good profiles after applying the quality control measures. It can be observed from the Figure 1 that the number of F3/C profiles are higher during 2007–2010 (low solar activity period) when all the satellites in the F3/C constellation are fully operational. The number of profiles in the later years decreased due to the operational failure of some of the F3/C satellites. Further, the electron density profiles from the Gravity Recovery and Climate Experiment (GRACE) radio occultation observations available during 2007–2015 and the International Reference Ionosphere (IRI-2016) model have been used for comparison to assess the performance of ANNIM.

2.1. Artificial Neural Networks

Our brain is more complex and mysterious object that ever studied by the scientists. The human brain consists of nearly 100 billion neurons which are massively interconnected into a parallel network to perform highly nonlinear tasks. The ANNs attempt to mimic the human brain (or biological neurons) to solve problems such as pattern recognition, clustering, generalization, linear and nonlinear data fitting, and time series prediction. The input-output relationship in neural networks is determined by the "strength of the signal" or "weights." McCulloch and Pitts (1943) explained the idea of neural network computation. According to the McCulloch and Pitts model, all neurons in the network are represented by a combination of logical functions. Widrow and Hoff (1960) introduced the Adaptive Linear Neuron (also known as Least Mean Squares rule) approach by adjusting the weight of the network, which significantly improved the learning ability of
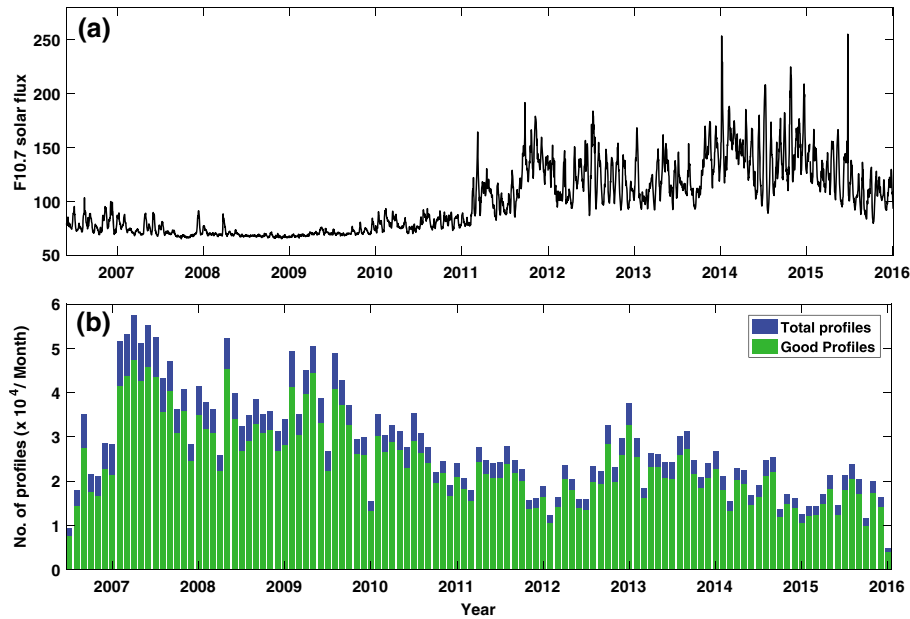
Figure 1. (a) Daily averaged $F_{10.7}$ solar flux during 2006–2015 and (b) data statistics showing the total number of F3/C profiles (green) per month and good profiles (blue) after quality control check.

neural networks. Rumelhart et al. (1986) has further introduced backpropagation of errors in the feed-forward neural networks, which increase the ability of the neural network computing to solve more complex problems. However, the learning speed was a problem at that time. Later, Jacobs (1988) improved the rate of convergence to the minimum least squares error of the neural networks by adapting the learning rate. Widrow and Lehr (1993) explained the applications of the adaptive neural networks, and its applications in various nonlinear problems. To solve nonlinear input-output relationship, feed-forward neural networks are very useful. A multilayer feed-forward neural network consists of three blocks, namely, input unit, hidden layer(s) and the output unit. The neural network outputs with "n" number of input neurons and "k" number of neurons can be written as (Krasnopolsky & Lin, 2012)

$$Y_q = g_{q0} + \sum_{j=1}^{k} g_{qj} \cdot \varphi\left(h_{j0} + \sum_{i=1}^{n} h_{ji} \cdot x_i\right) \qquad (1)$$

where $q = 1, 2, \ldots, m$ and $\varphi\left(h_{j0} + \sum_{i=1}^{n} h_{ji} \cdot x_i\right)$ represents an individual neuron with a nonlinear activation function φ. Here g and h denote the fitting parameter of the neural network. Flow diagram of a feed-forward neural network with error backpropagation algorithm is shown in Figure 2. Training of the network is done in
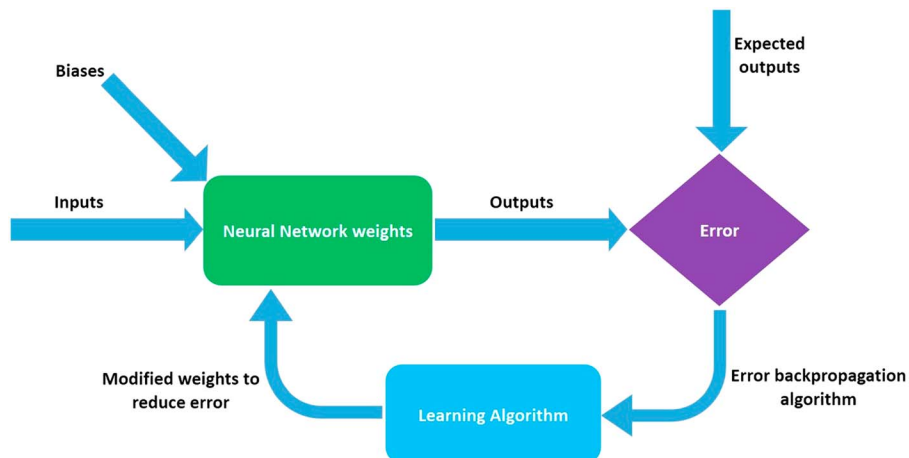

Figure 2. Flow diagram of a feed-forward neural network with error backpropagation algorithm.
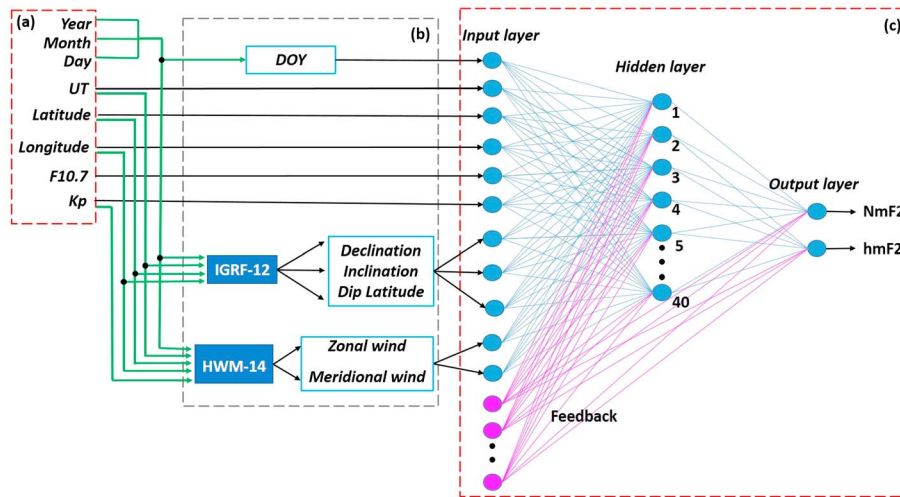
Figure 3. Configuration of Artificial Neural Network used in the present study. (a) Primary inputs to the neural network. (b) Calculation of additional inputs using IGRF-12 and HWM-14. (c) Architecture of feed-forward neural network with error backpropagation.

four steps: (i) initialization of weights and biases, (ii) feed forward, (iii) error backpropagation, and then (iv) updating the weights and biases. During the initial stage of learning, some random weights are assigned to the network. In the next stage (feed-forward), each input unit (x_i), receives a signal along with assigned weights, passes through each of the hidden nodes ($H_1, H_2, …, H_{40}$). Then, each unit in the hidden layer(s) calculates the activation function for each input parameter and weight and sends its signal to the output layer. The output layer computes the activation function to get the response of the network. In the third stage, the error is computed by comparing the expected output with the calculated output and backpropagated to all nodes in the previous layer(s). During the final stage, weights and biases are updated according to the estimated error factor. As shown in Figure 2, these steps are iteratively repeated in successive epochs until the network converges to the minimum least square error.

2.2. Neural Network Architecture and Training Method

In this study, the ANN is aimed to create a multivariate regression model to predict the ionospheric parameters such as F_2 layer peak electron density (N_mF_2) and peak height (h_mF_2). The MATLAB-based Levenberg-Marquardt (LM) algorithm (Levenberg, 1944; Marquardt, 1963) has been used to train the neural network. Though this method requires more computational memory, it takes less computation time. Figure 3 shows the block diagram and architecture of the neural network that used in the present study. The primary inputs used in our model are date (YYYY/MM/DD) or day number (DDD), time (Universal Time, UT), latitude, longitude, $F_{10.7}$ solar flux, and Kp index, shown in Figure 3a. These inputs also serve as inputs to the horizontal wind model (HWM-2014) (Drob et al., 2015) to compute zonal and meridional winds and International Geophysical Reference Field (IGRF-2012) model to calculate inclination, declination and dip latitude. These model computations of winds and geomagnetic field configurations are taken care by an internal subroutine in the program (gray box, Figure 3b). After performing several test runs and analyzing the regression values, we found that the architecture with one hidden layer that contains 40 neurons is suitable for our study. The final architecture of the feed-forward neural network with one input layer, one hidden layer with 40 neurons, and one output layer is shown in Figure 3c. During the training process of neural networks, the total data is divided into three sets, namely, training, validation, and testing. The training data set is used to obtain the nonlinear relationship between input parameters and the target parameters (N_mF_2 and h_mF_2) and compute the weights. The validation set (which is not used for training purpose) is used to optimize the neural network performance by estimating the errors and avoiding the overfitting of model parameters. The errors estimated during the validation are further used in the network to check if the errors are within the permissible range. The testing data set is an independent data that is not used in the training but used to assess the network performance only. In the present analysis, nearly 70% of the global F3/C data during the period from 2006 to 2015 is used for training, 15% of data is used for validating the network, and the remaining 15% of data is used for testing the neural network. We initially trained our neural network with entire global data set of
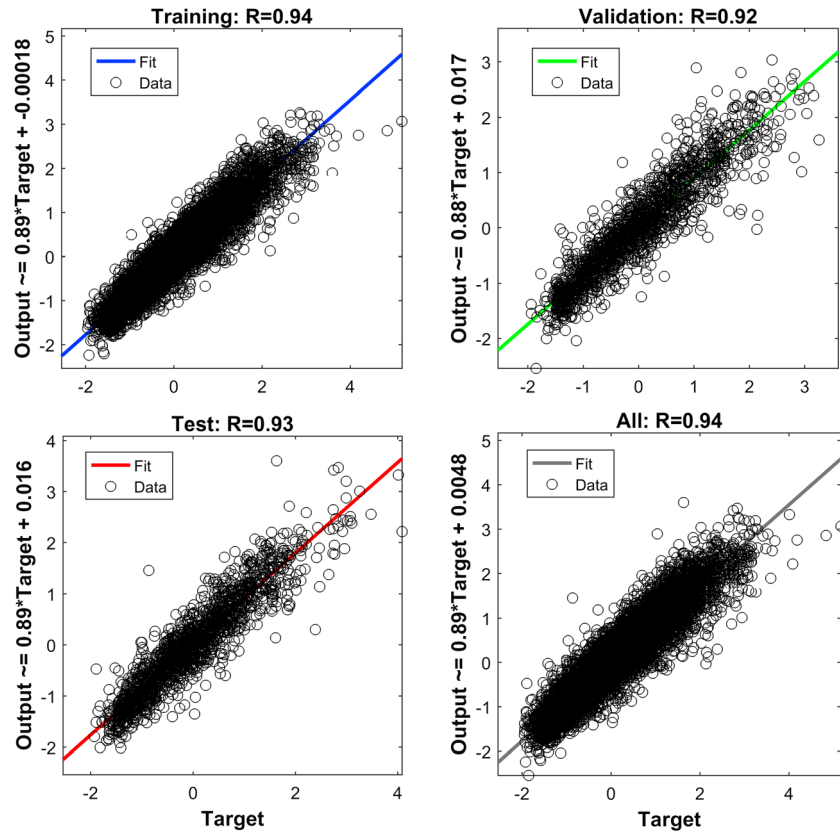
Figure 4. Linear regression between the normalized target parameters and ANN output during (a) training, (b) validation, and (c) testing phases for the spatial grid of 0–10°N latitude and 0–20°E longitude. (d) The linear regression between the predicted and target parameters for all the data.

F3/C with the above mentioned input parameters and found that the regression value (R) between the predicted and target parameters is 0.88.

To further improve the regression of the neural network, we have adopted a gridded neural network, rather than feeding the entire global data to a single neural network. In this approach, we divided the entire global data into small spatial grids of size 20° longitude × 10° latitude and the data in each grid are trained using the neural networks separately. Our basic idea is to get an individually trained neural network for each 20° longitude × 10° latitude spatial grid around the globe using the same architecture shown in Figure 3. As mentioned above, 70%, 15%, and 15% of data in each grid are used for training, validation, and testing of neural network, respectively. For example, Figure 4 shows the regression coefficient (R) between normalized target parameters (N_mF_2 and h_mF_2) and the predicted output parameters during training, validation, and testing steps for a spatial grid of 0–10°N latitude and 0–20°E longitude. Figure 4 (bottom right) shows the regression between the predicted and target parameters for all the data. The colored solid lines represent the fit of the corresponding predicted values and the regression values are shown on the top of each panel. With this gridded neural network approach, the regression in each spatial grid has significantly improved compared to the single neural network approach on global data. One can see that the overall regression value is nearly 0.93, which has significantly improved compared to the single neural network approach (0.88). Finally, a cluster of 324 trained neural networks, one for each spatial (20° longitude × 10° latitude) grid, were developed. A front-end MATLAB routine that selects the appropriate neural network based on the input parameters is further developed to combine the set of 324 neural networks and build a two-dimensional (2-D) model that can predict the ionospheric F_2 layer peak parameters (N_mF_2 and h_mF_2), globally.

3. Results

The learning efficiency of the above neural network configuration and performance of this Artificial Neural Network-based Ionospheric Model (ANNIM) to predict the N_mF_2 and h_mF_2 is evaluated in this section. For
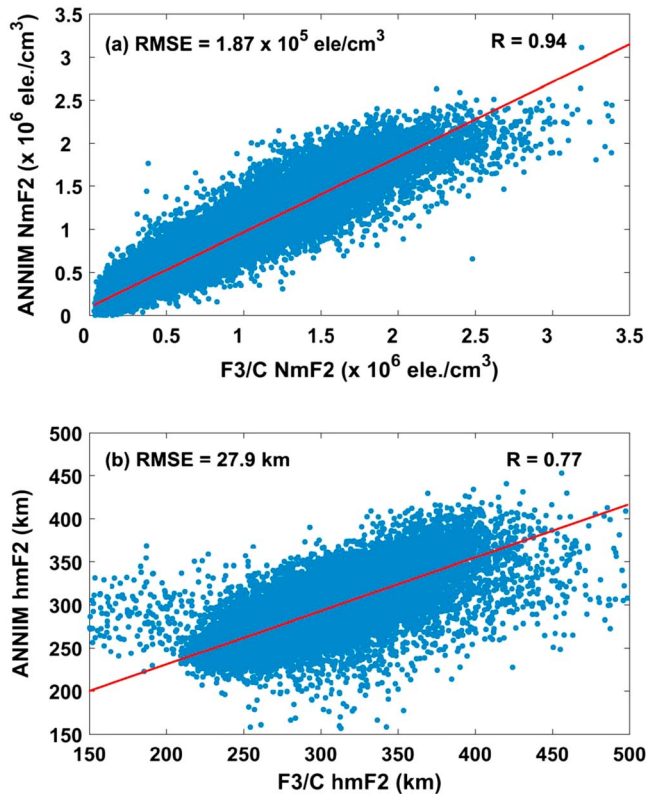
Figure 5. The linear regression between ANNIM predictions and the actual F3/C for (a) N_mF_2 and (b) h_mF_2 under March equinox (day number = 80 ± 20), moderate solar activity ($F_{10.7}$ = 120 ± 10), and quiet geomagnetic ($Kp \leq 3$) conditions.

this purpose, the N_mF_2 and h_mF_2 data from the F3/C observations under March equinox (day number = 80 ± 20 days) with moderate solar activity ($F_{10.7}$ solar flux = 120 ± 10 solar flux unit (sfu)) and quiet geomagnetic activity ($Kp \leq 3$) conditions were selected from the entire available F3/C data set. A total of ~30,000 data points have been selected that meet the above selection criteria. Also, it should be noted that the selected N_mF_2 and h_mF_2 data from F3/C that comprise different latitudes, longitudes, local times, and years, however, meet the selection criteria of day number = 80 ± 20 days, $F_{10.7}$ solar flux = 120 ± 10 sfu and $Kp \leq 3$. Now, the ANNIM has been run to predict the N_mF_2 and h_mF_2 values for the same latitudes, longitudes, and local times of actual F3/C data with day number = 80, $F_{10.7}$ = 120 sfu and Kp = 3. The ANNIM predicted N_mF_2 and h_mF_2 values are compared with the actual F3/C data in Figures 5a and 5b, respectively. As can be observed from Figures 5a and 5b the predicted N_mF_2 and h_mF_2 by ANNIM are well correlated with the actual F3/C data. The linear regression between ANNIM and F3/C data gives the regression coefficients (R) of 0.94 for N_mF_2 and 0.77 for h_mF_2. The RMS (root-mean-square) errors of the ANNIM predictions are 1.87 x 10⁵ el/cm³ for N_mF_2 and 27.9 km for h_mF_2. These results indicate that the learning capability of the proposed neural network architecture and the performance of ANNIM are very good for N_mF_2 and reasonably good for h_mF_2.

The spatial and temporal variations of N_mF_2 and h_mF_2 predicted by ANNIM are further examined in comparison with the actual F3/C data. Both the ANNIM-predicted and F3/C data of N_mF_2 and h_mF_2 (above data, shown in Figure 5) are binned into 2.5° geographic latitude, 2.5° dip latitude, 5° geographic longitude, 30 min local time intervals to construct the spatial and temporal maps of N_mF_2 and h_mF_2. For example, Figures 6a and 6b show the geographic latitude and longitude variations of N_mF_2 derived from ANNIM and F3/C, respectively, at a fixed local time of 12 LT. A 10-point smoothing is applied on both ANNIM and F3/C data, and in both latitude and longitude directions to construct the smooth spatial variation maps of N_mF_2. One can observe from the Figures 6a and 6b that the
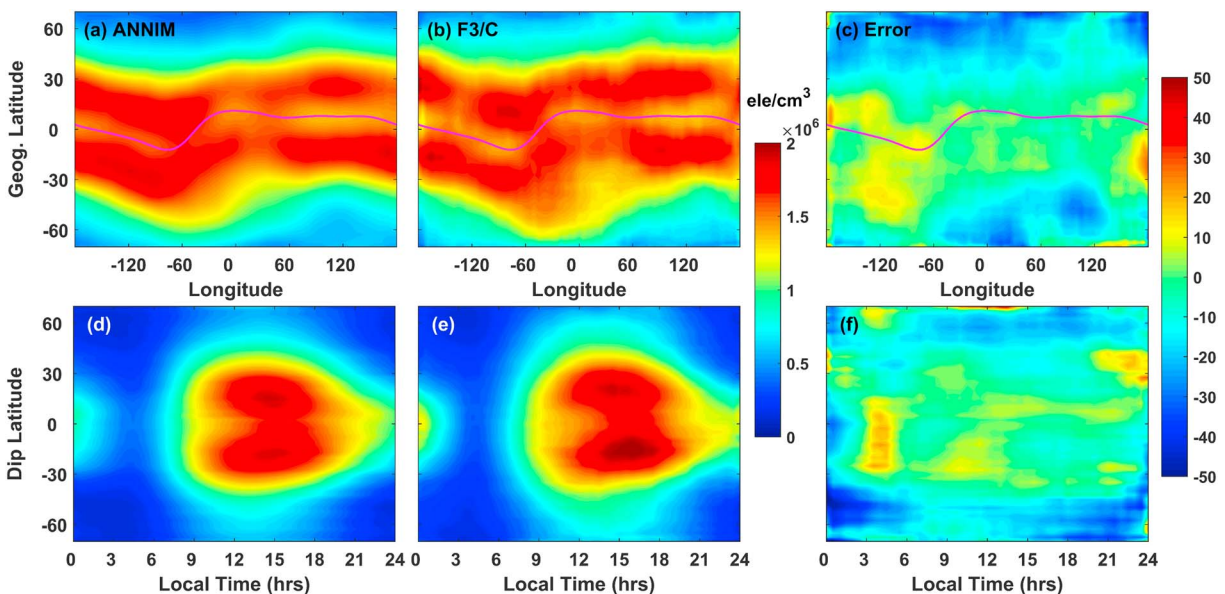

Figure 6. Geographic latitude and longitude variations of N_mF_2 derived from (a) ANNIM, (b) F3/C, and (c) percentage of error at 12 LT during March equinox. The local time and dip latitude variation of zonal mean (longitudinally average) N_mF_2 derived from (d) ANNIM and (e) F3/C and (f) percentage of error.
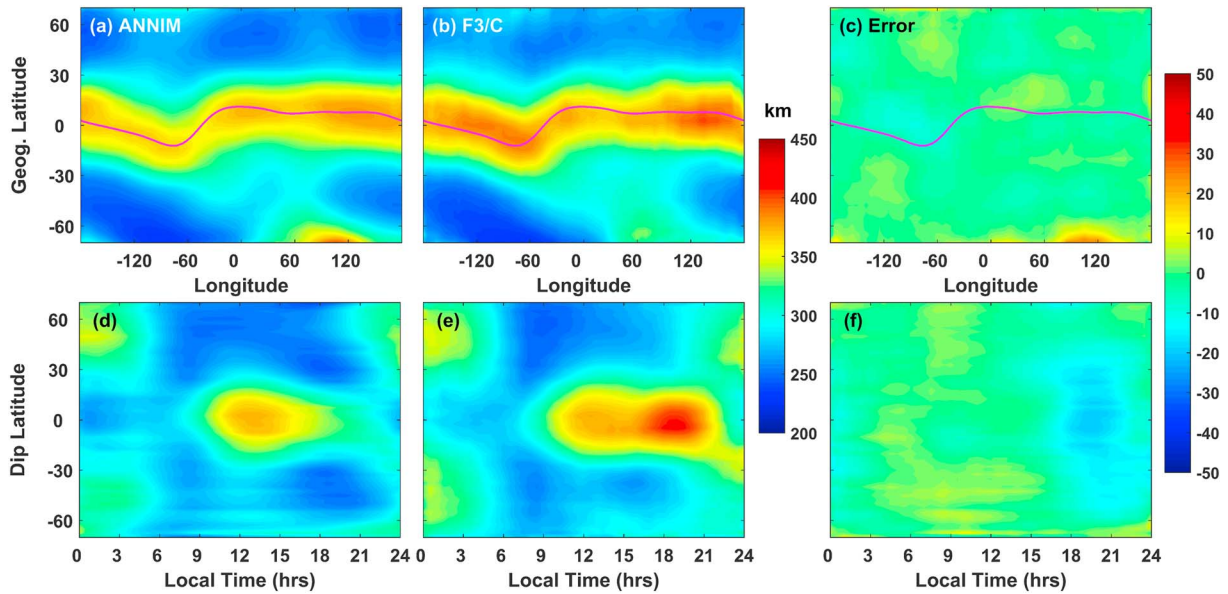
Figure 7. Geographic latitude and longitude variations of h_mF_2 derived from (a) ANNIM, (b) F3/C, and (c) percentage of error at 12 LT during March equinox. The local time and dip latitude variation of zonal mean (longitudinally average) h_mF_2 derived from (d) ANNIM and (e) F3/C and (f) percentage of error.

geographic latitude and longitudinal variations of N_mF_2 predicted by ANNIM are in good agreement with the original F3/C data indicating that the ANNIM has well captured the spatial variation of N_mF_2. Figure 6c shows the error in the model predicted N_mF_2 when compared to original F3/C data expressed in percentage, as given by

$$\text{Percentage of Error } (E) = \frac{\text{ANNIM} - \text{F3/C data}}{\text{F3/C data}} \times 100 \qquad (2)$$

From Figure 6, one can see that the percentage error remains below 15% at most locations. However, the ANNIM appears to underestimate the N_mF_2 at high-latitudes where the error increases to ~20–25%. The slightly higher percentage of error at high latitudes can partly be due to low background N_mF_2 values and low-solar activity data bias in the training data set used in the present model, will be discussed later in section 4.

Similarly, Figure 6d shows the local time and dip latitude variation of zonal mean (longitudinally average) N_mF_2 derived from ANNIM. From the Figure 6d, one can see that the local time and dip latitude variations of N_mF_2, such as, low values during predawn hours, steadily increasing after sunrise, reaching maximum around noon and afternoon hours with a well-developed equatorial ionization anomaly and decreasing after sunset have been successfully captured by the model. Figure 6e shows the similar local time and dip latitude variations of N_mF_2 constructed from the actual F3/C. Comparison of Figures 6d and 6e clearly indicates that the model predicted N_mF_2 values and its local time and dip latitudes variations are in good agreement with the F3/C data. Figure 6f shows that the error in the model predicted N_mF_2 with respect to original F3/C data is small and mostly remains below ~15–20%. The ANNIM-predicted N_mF_2 also show error greater than 20% at some times, for example, at low latitudes during the predawn hours of 3–5 LT (overestimated) and at southern middle-to-high latitudes around midnight (underestimated). These large errors can also be partly due to very low background ionization which could often magnify the error because of low denominator value in equation (2).

Figure 7 is similar to that of Figure 6, however, presents variations of h_mF_2. One can observe from Figure 7 that the ANNIM has well captured the spatial and temporal variations of h_mF_2 and generally in good agreement with the F3/C observations. The percentage error remains to be small (less than 10%) at all latitudes, longitudes, and local times except during the postsunset hours at equatorial and low latitudes (18–21 LT in Figure 7f). The model underestimates the h_mF_2 at equatorial and low latitudes during the postsunset hours when compared to F3/C data. The enhanced h_mF_2 values in the F3/C data (Figure 7e) during the
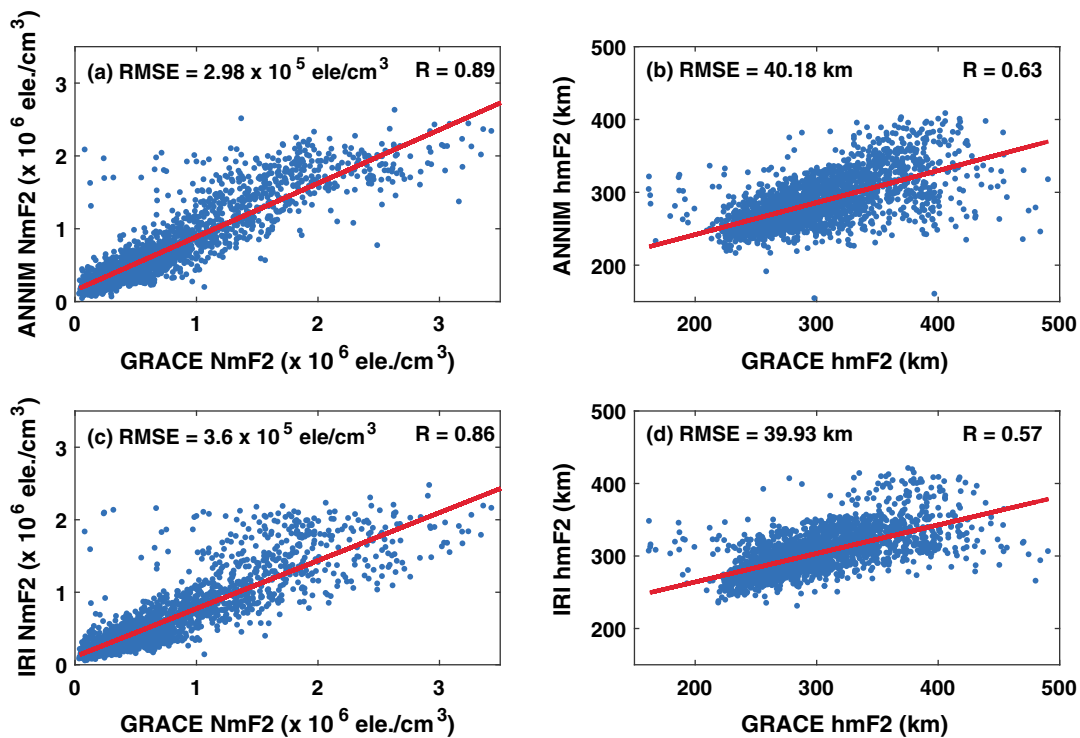
Figure 8. Linear regression between ANNIM predictions and independent GRACE radio occultation observations for (a) N_mF_2 and (b) h_mF_2. Linear regression between IRI-2016 model predictions and GRACE RO observations for (c) N_mF_2 and (d) h_mF_2.

postsunset hours at equatorial latitudes can be attributed to postsunset height rise of equatorial F layer due to prereversal enhancement in the zonal electric field (Farley et al., 1986; Park et al., 2010; Rishbeth, 1971). However, the ANNIM fails to capture this feature around postsunset hours.

After the comparisons of ANNIM predictions with the F3/C data, it is also important to compare the model results with an independent data set that was not used in the present model. For this purpose, the global N_mF_2 and h_mF_2 data from the GRACE-RO profiles were obtained under similar conditions of day number = 80 ± 20 days, $F_{10.7}$ solar flux = 120 ± 10 sfu, and $Kp \leq 3$ from the available GRACE data during the period 2007–2015. Now the ANNIM as well as IRI-2016 models has been run for the given latitudes, longitudes, and UT times of actual GRACE data points with day number = 80, $F_{10.7}$ = 120, and Kp = 3. The ANNIM and IRI-2016 model predictions of N_mF_2 and h_mF_2 are compared with the actual GRACE data in Figure 8. Figures 8a and 8b show the ANNIM predictions, and Figures 8c and 8d show the IRI-2016 model predictions with respect to the GRACE data. Figures 8a and 8c (Figures 8b and 8d) show the N_mF_2 (h_mF_2) comparisons. It can be seen from the Figures 8a and 8b that the ANNIM predictions are linearly correlated with the GRACE data with the regression coefficients values of 0.89 and 0.63 for N_mF_2 and h_mF_2, respectively. The RMS error is 2.98×10^5 el/cm^3 for N_mF_2 and 40.18 km for h_mF_2 in comparison with the independent GRACE data. Further, the IRI-2016 model predictions of N_mF_2 and h_mF_2 (Figures 8c and 8d) also linearly correlated with GRACE data with the regressions coefficients of 0.86 and 0.57 for N_mF_2 and h_mF_2, respectively. The RMS error in IRI predicted N_mF_2 is slightly higher (3.6×10^5 el/cm^3) and that for h_mF_2 is nearly same (39.93) compared to ANNIM. Therefore, from the results presented in Figure 8, one can conclude that the ANNIM predictions of N_mF_2 and h_mF_2 are reasonably good and nearly comparable with IRI model predictions. However, the ANNIM gives slightly better correlation (3%) for N_mF_2 and h_mF_2 (6%) than by IRI-2016 with respect to the independent GRACE data.

With a view to further examine the model response during the solstices, the ANNIM has been run for similar conditions ($F_{10.7}$ = 120 sfu and Kp = 3) for June solstices (day number = 172) and December solstices (day number = 354) and compared with F3/C data. The IRI model also has been run with the same inputs to further compare the ANNIM. For example, Figure 9 shows the longitudinal and latitudinal variation of N_mF_2 at fixed local time of 12 LT during June (a–c) and December (d–f) solstices. Figures 9a and 9d represent ANNIM results,
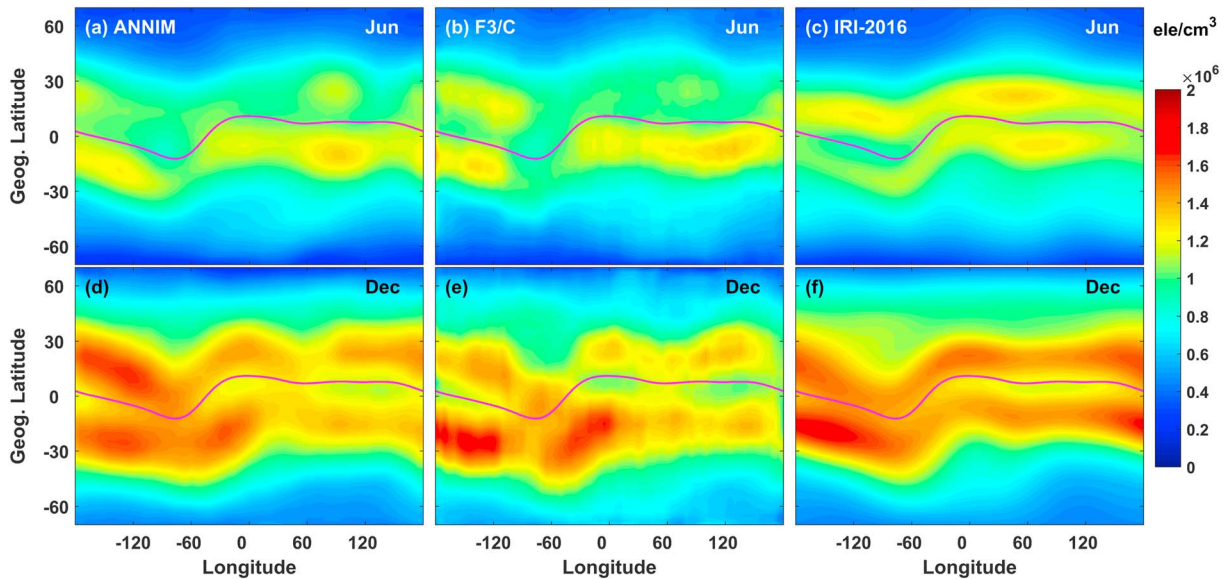
Figure 9. The global ionospheric N_mF_2 maps generated around local noon (12 LT) by using (a, d) ANNIM, (b, e) F3/C data, and the (c, f) IRI-2016 model during June (Figures 9a–9c) and December (Figures 9d–9f) solstices.

Figures 9b and 9e represent F3/C data, and Figures 9c and 9f represent the IRI-2016. From Figure 9, one can clearly observe that the longitudinal and latitudinal variations of derived from ANNIM are in good agreement with the F3/C data during both the solstices. Further, it can also be observed that the N_mF_2 is globally large during the December solstice (Figures 9d–9f) when compared to June solstices (Figures 9a–9c), which is popularly known as ionospheric annual anomaly (Berkner & Wells, 1938; Rishbeth & Muller-Wodarg, 2006; Sai Gowtam & Tulasi Ram, 2017; Yonezawa, 1971; Zeng et al., 2008). This indicates that the ANNIM has successfully captured the seasonal and annual variations of N_mF_2. Further, the longitudinal and latitudinal variations predicted by ANNIM are nearly comparable to those predicted by the IRI-2016 model. However, IRI-2016 model gives relatively smoother longitudinal variations. The fine longitudinal structures around equatorial ionization anomaly region appear to be better represented by ANNIM than in IRI-2016 when compared with the F3/C data. This is somewhat expected as the ANNIM is primarily developed based on the F3/C data.
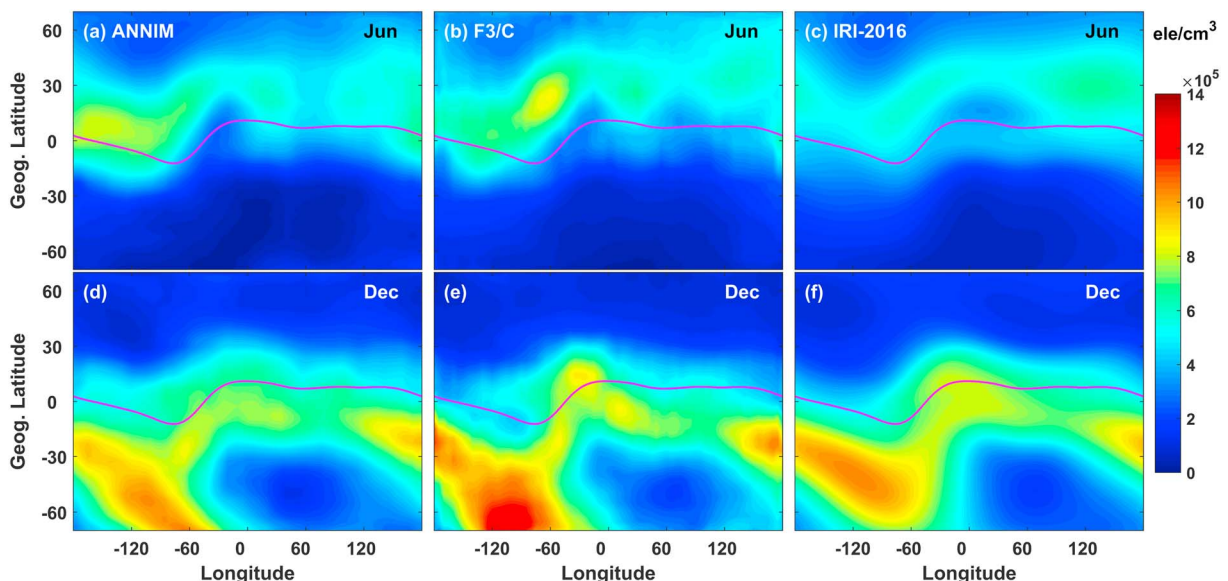

Figure 10. The global ionospheric N_mF_2 maps generated around local midnight (00 LT) by using (a, d) ANNIM, (b, e) F3/C data, and the (c, f) IRI-2016 model during June (Figures 10a–10c) and December (Figures 10d–10e) solstices.

Figure 10 is similar to Figure 9 except for midnight local time (00 LT) conditions. It can be seen from these figures that the N_mF_2 is generally high in the respective summer hemispheres (Northern Hemisphere during June and Southern Hemisphere during December) at low and middle latitudes. This feature is generally known as midlatitude summer nighttime anomaly (MSNA) in the Northern Hemisphere (Lin et al., 2010; Thampi et al., 2009) and its Southern Hemispheric counterpart is popularly known as Weddell Sea Anomaly (WSA) (Bellchambers & Piggott, 1958; He et al., 2009). These midlatitude nighttime enhancements of N_mF_2 in the summer hemispheres are generally attributed to the combined effects of equatorward neutral winds in the presence of geomagnetic field configuration (Liu et al., 2010). Nevertheless, the ANNIM has successfully reproduced these midlatitude nighttime phenomena of MSNA and WSA. The ANNIM results are also similar to that of IRI-2016; however, the ANNIM better resembles with the F3/C data as expected.

4. Summary and Discussion

An ANN-based ionospheric model (ANNIM) to predict the ionospheric F_2 layer peak density (N_mF_2) and height (h_mF_2) has been developed using the long-term (2006–2015) and global data of F3/C radio occultation observations. The global F3/C data have been divided in to spatial grids of 20° longitude × 10° latitude, and the data in each grid were trained using the same neural network architecture given in Figure 3. The basic idea behind dividing the global data in to smaller spatial grids is to reduce the spatial variability of data in each grid. Training the neural network over smaller spatial grids improves the learning and adoptability by the neural network to the given set of input parameters. Accordingly, the linear regression value has been increased from 0.88 for single neural network approach on global data to 0.93 for a neural network on a spatial grid of 20° longitude × 10° latitude (Figure 4). However, dividing the global data into too smaller spatial grids causes an increase in the number of neural networks. Hence, there is a trade-off between the number of neural networks and the size of the spatial grids. In the present study, we adopted a spatial grid size of 20° longitude × 10° latitude and the data in each spatial grid are separately trained. Therefore, this model comprises of 324 trained neural networks, one for each grid. Finally, the set of 324 trained neural networks combined through a front-end code to build the two-dimensional (2-D) model (ANNIM) that can predict the N_mF_2 and h_mF_2.

In this pilot study, the learning efficiency of the proposed neural network approach and the performance of ANNIM under moderate solar activity ($F_{10.7}$ = 120 sfu) and quiet geomagnetic ($Kp \leq 3$) conditions have been evaluated in comparison with actual F3/C data. The linear regression coefficients between the ANNIM results and actual F3/C data are 0.93 for N_mF_2 and 0.77 for h_mF_2, and the RMS errors are 1.87×10^5 el/cm^3 for N_mF_2 and 27.9 km for h_mF_2 (Figure 5). The comparisons of ANNIM results and actual F3/C data shown in Figures 6, 7, 9, and 10 clearly indicate that the local time, latitude, longitude, and seasonal variations of N_mF_2 and h_mF_2 were well captured by the ANNIM. The estimated error in N_mF_2 by ANNIM predictions is mostly below 15% with respect to F3/C data; however, the error is sometimes greater than 20%, particularly, at local times and latitudes where the background ionization is very low (Figure 6). It should also be noted that the actual F3/C data used in Figures 6 and 7 are pooled from the entire database that meets the criteria of day number = 80 ± 20 days, $F_{10.7}$ solar flux = 120 ± 10 sfu, and $Kp \leq 3$ to construct the spatial and temporal distribution maps. Hence, there could be an inherent variability (such as day-to-day) that already exists in the N_mF_2 and h_mF_2 values of F3/C data points that are pooled from a range of day number (80 ± 20 days), $F_{10.7}$ (120 ± 10), and Kp (≤ 3) values. On the other hand, the ANNIM has been run with the fixed inputs of day number = 80, $F_{10.7}$ = 120 sfu, and Kp = 3 while comparison. Therefore, given the differences in the ANNIM runs and the actual F3/C data points, an error of 15–20% would be reasonable and/or encouraging.

The error in the predicted h_mF_2 by ANNIM is mostly below 10% except during the postsunset hours where the ANNIM underestimates the h_mF_2 around equatorial and low latitudes (Figures 7d–7f). The equatorial F layer often elevated (h_mF_2 increases) during the postsunset hours due to prereversal enhancement in the zonal electric field as can be seen from the F3/C data in Figure 7e. However, the ANNIM fails to capture this feature (Figures 7d and 7f). One of the reasons behind this failure by ANNIM, perhaps, is the relatively smaller number of h_mF_2 points at equatorial and low latitudes that reflect the postsunset enhancement in a given spatial grid (during the training). Also, lack of input parameter (such as zonal electric field) that drives the postsunset enhancement of h_mF_2 in the present model could be another reason. Reducing the spatial grid size at equatorial latitudes and training with an additional input of zonal electric field may, perhaps, improve the

response of model during the postsunset hours which would be carried out in our subsequent studies. Further, the comparison with an independent data set of GRACE radio occultation observations in Figure 8 shows that the RMS error is slightly increased for both N_mF_2 and h_mF_2. However, the ANNIM predictions are still good and nearly comparable with the IRI model predictions. Further, the ANNIM predictions show slightly better (3% for N_mF_2 and 6% for h_mF_2) with GRACE data than the IRI-2016 model.

Nevertheless, the ANNIM has well captured the local time, latitude, longitude and seasonal variations as presented in Figures 6, 7, 9, and 10. Further, the ANNIM has successfully reproduced the large-scale ionospheric features such as ionospheric annual anomaly (Figure 9) and midlatitude nighttime enhancements such as MSNA and WSA (Figure 10). Also, the N_mF_2 variations predicted by ANNIM are nearly comparable with the IRI-2016 model, however, better represents the finer spatial structures with respect to F3/C data (Figures 9 and 10). This is expected as the ANNIM is primarily developed based on F3/C data. These results indicate that the neural networks used in the present study are appropriately trained and the two-dimensional ANNIM has well reproduced the spatial and temporal variations of ionospheric N_mF_2 and h_mF_2.

With these promising results by ANNIM, further studies will be focused on optimizing the model. There is a lot of scope to improve the model, particularly, N_mF_2 response at high latitudes and h_mF_2 response during the postsunset hours where the error becomes significant as discussed earlier. It should also be noted that the quantum of available F3/C data that is used to train the ANN is heavily weighted during the relatively low solar activity years (2007–2010) where the $F_{10.7}$ solar flux is mostly below 100 sfu (Figure 1). However, we purposefully compared the ANNIM predictions at $F_{10.7}$ is around 120 sfu in order to examine the model performance at moderately higher solar flux levels where the quantum of data used for training of ANN is relatively small. The underestimation of N_mF_2 at high latitudes (Figure 6) and h_mF_2 during postsunset hours around equatorial and low latitudes (Figure 7) by ANNIM can partly be attributed for these differences in solar flux conditions as the larger ion production and higher postsunset enhancement of h_mF_2 is expected during the higher solar activity levels (Tulasi Ram et al., 2006). Despite this low-solar activity bias in F3/C data, the ANNIM gives promising results at moderate solar flux levels, and also, there is a good scope for the improvement of model provided more data at higher solar activity levels is included in the ANN training. Further, the ANNIM response during the disturbed space weather and geomagnetic activity periods needs to be carefully evaluated with independent data sets, which will be carried out in our subsequent reports. Finally, the ANNIM can be further extended to model the total ionospheric vertical electron density profile, and a complete three-dimensional (3-D) model would be developed using the global RO data from F3/C and other missions such as CHAMP, GRACE, and the upcoming FORMOSAT-7/COSMIC-2 (Lee et al., 2013; Yue et al., 2014).

References

Altinay, O., Tulunay, E., & Tulunay, Y. (1997). Forecasting of ionospheric critical frequency using neural networks. *Geophysical Research Letters*, *24*(12), 1467–1470. https://doi.org/10.1029/97GL01381

Anderson, D. N., Buonsanto, M. J., Codrescu, M., Decker, D., Fesen, C. G., Fuller-Rowell, T. J., … Sojka, J. J. (1998). Intercomparison of physical models and observations of the ionosphere. *Journal of Geophysical Research*, *103*(A2), 2179–2192. https://doi.org/10.1029/97JA02872

Athieno, R., Jayachandran, P. T., & Themens, D. R. (2017). A neural network-based f_oF_2 model for a single station in the polar cap. *Radio Science*, *52*, 784–796. https://doi.org/10.1002/2016RS006192

Bailey, G. J., & Balan, N. (1996). A low-latitude ionosphere-plasmasphere model. In R. W. Schunk (Ed.), *STEP handbook on ionospheric models*, (pp. 173–206). Logan: Utah State University.

Bailey, G. J., Balan, N., & Su, Y. Z. (1997). The Sheffield University plasmasphere-ionosphere model—A review. *Journal of Atmospheric and Solar - Terrestrial Physics*, *59*(13), 1541–1552. https://doi.org/10.1016/S1364-6826(96)00155-1

Bellchambers, W. H., & Piggott, W. R. (1958). Ionospheric measurements made at Halley Bay. *Nature*, *182*(4649), 1596–1597. https://doi.org/10.1038/1821596a0

Berkner, L. V., & Wells, H. W. (1938). Non-seasonal change of F_2-region ion density. *Terrestrial Magnetism and Atmospheric Electricity*, *43*(1), 15–36. https://doi.org/10.1029/TE043i001p00015

Bilitza, D. (2001). International reference ionosphere 2000. *Radio Science*, *36*(2), 261–275. https://doi.org/10.1029/2000RS002432

Daniell, R. E. Jr., Brown, L. D., Anderson, D. N., Fox, M. W., Doherty, P. H., Decker, D. T., … Schunk, R. W. (1995). Parameterized ionospheric model: A global ionospheric parameterization based on first principles models. *Radio Science*, *30*(5), 1499–1510. https://doi.org/10.1029/95RS01826

Dmitriev, A. V., & Suvorova, A. V. (2000). Three-dimensional artificial neural network model of the dayside magnetopause. *Journal of Geophysical Research*, *105*(A8), 18,909–18,918. https://doi.org/10.1029/2000JA900008

Drob, D. P., Emmert, J. T., Meriwether, J. W., Makela, J. J., Doornbos, E., Conde, M., … Klenzing, J. H. (2015). An update to the horizontal wind model (HWM): The quiet time thermosphere. *Earth and Space Science*, *2*(7), 301–319. https://doi.org/10.1002/2014EA000089

Farley, D. T., Bonelli, E., Fejer, B. G., & Larsen, M. F. (1986). The pre- reversal enhancement of the zonal electric field in the equatorial ionosphere. *Journal of Geophysical Research*, *91*(A12), 13,723–13,728. https://doi.org/10.1029/JA091iA12p13723

Fuller-Rowell, T. J., Rees, D., Quegan, S., Moffett, R. J., Codrescu, M. V., & Millward, G. H. (1996). A coupled thermosphere-ionosphere model (CTIM). In R. W. Schunk (Ed.), *STEP: Handbook of ionospheric models* (pp. 217–238). Logan, Utah: Utah State University.

He, M., Liu, L., Wan, W., Ning, B., Zhao, B., Wen, J., … Le, H. (2009). A study of the Weddell Sea anomaly observed by FORMOSAT-3/COSMIC. *Journal of Geophysical Research*, *114*, A12309. https://doi.org/10.1029/2009JA014175

Hochegger, G., Nava, B., Radicella, S. M., & Leitinger, R. (2000). A family of ionospheric models for different uses. *Physics and Chemistry of the Earth, Part C: Solar, Terrestrial & Planetary Science*, *25*(4), 307–310.

Huang, Z., & Yuan, H. (2014). Ionospheric single-station TEC short-term forecast using RBF neural network. *Radio Science*, *49*, 283–292. https://doi.org/10.1002/2013RS005247

Huba, J. D., Joyce, G., & Fedder, J. A. (2000). Sami2 is another model of the ionosphere (SAMI2): A new low-latitude ionosphere model. *Journal of Geophysical Research*, *105*(A10), 23,035–23,053. https://doi.org/10.1029/2000JA000035

Jacobs, R. A. (1988). Increased rate of convergence through learning rate adaption. *Neural Networks*, *2*, 100–117.

Krasnopolsky, V. M., & Lin, Y. (2012). A neural network nonlinear multimodel ensemble to improve precipitation forecasts over continental US. *Advances in Meteorology*, *2012*, 649450, 1–11. https://doi.org/10.1155/2012/649450

Kumluca, A., Tulunay, E., Topalli, I., & Tulunay, Y. (1999). Temporal and spatial forecasting of ionospheric critical frequency using neural networks. *Radio Science*, *34*(6), 1497–1506. https://doi.org/10.1029/1999RS900070

Lamming, X., & Cander, L. R. (1999). Monthly median f_oF_2 modelling COST 251 area by neural networks. *Physics and Chemistry of the Earth - Part C*, *24*, 349–354.

Lee, I. T., Tsai, H. F., Liu, J. Y., Lin, C. H., Matsuo, T., & Chang, L. C. (2013). Modelling impact of FORMOSAT-7/COSMIC-2 mission on ionospheric space weather monitoring. *Journal of Geophysical Research: Space Physics*, *118*, 6518–6523. https://doi.org/10.1002/jgra.50538

Lei, J., Syndergaard, S., & Burns, A. G. (2007). Comparison of COSMIC ionospheric measurements with ground-based observations and model predictions: Preliminary results. *Journal of Geophysical Research*, *112*, A07308. https://doi.org/10.1029/2006JA012240

Levenberg, K. (1944). A method for the solution of certain non-linear problems in least squares. *Quarterly of Applied Mathematics*, *2*(2), 164–168. https://doi.org/10.1090/qam/10666

Lin, C. H., Liu, C. H., Liu, J. Y., Chen, C. H., Burns, A. G., & Wang, W. (2010). Midlatitude summer nighttime anomaly of the ionospheric electron density observed by FORMOSAT-3/COSMIC. *Journal of Geophysical Research*, *115*, A03308. https://doi.org/10.1029/2009JA014084

Liu, H., Thampi, S. V., & Yamamoto, M. (2010). Phase reversal of the diurnal cycle in the midlatitude ionosphere. *Journal of Geophysical Research*, *115*, A01305. https://doi.org/10.1029/2009JA014689

Ma, X. F., Maruyama, T., Ma, G., & Takeda, T. (2005). Three-dimensional ionospheric tomography using observation data of GPS ground receivers and ionosonde by neural network. *Journal of Geophysical Research*, *110*, A05308. https://doi.org/10.1029/2004JA010797

Macpherson, K. P., Conway, A. J., & Brown, J. C. (1995). Prediction of solar and geomagnetic activity data using neural networks. *Journal of Geophysical Research*, *100*(A11), 21,735–21,744. https://doi.org/10.1029/95JA02283

Marquardt, D. W. (1963). An algorithm for the least-squares estimation of nonlinear parameters. *SIAM Journal of Applied Mathematics*, *11*(2), 431–441. https://doi.org/10.1137/0111030

McCulloch, W. S., & Pitts, W. H. (1943). A logical calculation of immanent in nervous activity. *Bulletin of Mathematical Biology*, *5*, 115–133.

Nava, B., Radicella, S. M., Leitinger, R., & Coisson, P. (2006). A near-real-time model-assisted ionosphere electron density retrieval method. *Radio Science*, *41*, RS6S16. https://doi.org/10.1029/2005RS003386

Oyeyemi, E. O., & Poole, A. W. V. (2004). Towards the development of a new global f_oF_2 empirical model using neural networks. *Advances in Space Research*, *34*(9), 1966–1972. https://doi.org/10.1016/j.asr.2004.06.010

Oyeyemi, E. O., Poole, A. W. V., & McKinnell, L. A. (2005). On the global model for f_oF_2 using neural networks. *Radio Science*, *40*, RS6011. https://doi.org/10.1029/2004RS003223

Park, J., Luhr, H., Fejer, B. G., & Min, K. W. (2010). Duskside F region dynamo currents: Its relationship with prereversal enhancement of vertical plasma drift. *Annales de Geophysique*, *28*(11), 2097–2101. https://doi.org/10.5194/angeo-28-2097-2010

Poole, A. W. V., & Poole, M. (2002). Long-term trends in f_oF_2 over Grahamstown using neural networks. *Annals of Geophysics*, *45*, 155–161.

Potula, B. S., Chu, Y.-H., Uma, G., Hsia, H.-P., & Wu, K.-H. (2011). A global comparative study on the ionospheric measurements between COSMIC radio occultation technique and IRI model. *Journal of Geophysical Research*, *116*, A02310. https://doi.org/10.1029/2010JA015814

Radicella, S. M., & Leitinger, R. (2001). The evolution of the DGR approach to model electron density profiles. *Advances in Space Research*, *27*(1), 35–40. https://doi.org/10.1016/S0273-1177(00)00138-1

Richmond, A. D., Ridley, E. C., & Roble, R. G. (1992). A thermosphere/ionosphere general circulation model with coupled electrodynamics. *Geophysical Research Letters*, *6*, 601–604.

Rishbeth, H. (1971). Polarization fields produced by winds in the equatorial F region. *Planetary and Space Science*, *19*(3), 357–369. https://doi.org/10.1016/0032-0633(71)%2090098-5

Rishbeth, H., & Muller-Wodarg, I. C. F. (2006). Why is there more ionosphere in January than in July? The annual asymmetry in the F_2-layer. *Annales de Geophysique*, *24*(12), 3293–3311. https://doi.org/10.5194/angeo-24-3293-2006

Roble, R. G., & Ridley, E. C. (1994). A thermosphere-ionosphere-mesosphere-electrodynamics general circulation model (TIME-GCM): Equinox solar cycle minimum simulations (30-500 km). *Geophysical Research Letters*, *21*(6), 417–420. https://doi.org/10.1029/93GL03391

Roble, R. G., Ridley, E. C., Richmond, A. D., & Dickinson, R. E. (1988). A coupled thermosphere/ionosphere general circulation model. *Geophysical Research Letters*, *15*(12), 1325–1328. https://doi.org/10.1029/GL015i012p01325

Rumelhart, D. E., Hinton, G. E., & Williams, R. (1986). Learning representations by back-propagating errors. *Nature*, *323*(6088), 533–536. https://doi.org/10.1038/323533a0

Sai Gowtam, V., & Tulasi Ram, S. (2017). Ionospheric winter anomaly and annual anomaly observed from Formosat-3/COSMIC Radio Occultation observations during the ascending phase of solar cycle 24. *Advances in Space Research*. https://doi.org/10.1016/j.asr.2017.03.017

Schreiner, W. S., Rocken, C., Sokolovskiy, S., Syndergaard, S., & Hunt, D. C. (2007). Estimates of the precision of GPS radio occultation from the COSMIC/FORMOSAT-3 mission. *Geophysical Research Letters*, *34*, L04808. https://doi.org/10.1029/2006GL027557

Schunk, R. W. (Ed.) (1996). *STEP: Handbook of ionospheric models*. Logan, Utah: Utah State University.

Schunk, R. W., Banks, P. M., & Raitt, W. J. (1976). Effects of electric fields and other processes upon the nighttime high-latitude F layer. *Journal of Geophysical Research*, *81*(19), 3271–3282. https://doi.org/10.1029/JA081i019p03271

Schunk, R. W., Raitt, W. J., & Banks, P. M. (1975). Effect of electric fields on the daytime high-latitude E and F regions. *Journal of Geophysical Research*, *80*(22), 3121–3130. https://doi.org/10.1029/JA080i022p03121

Schunk, R. W., & Walker, J. C. G. (1973). Theoretical ion densities in the lower ionosphere. *Planetary and Space Science*, *21*(11), 1875–1896. https://doi.org/10.1016/0032-0633(73)90118-9

Shin, D.-K., Lee, D.-Y., Kim, K.-C., Hwang, J., & Kim, J. (2016). Artificial neural network prediction model for geosynchronous electron fluxes: Dependence on satellite position and particle energy. *Space Weather*, *14*, 313–321. https://doi.org/10.1002/2015SW001359

Shunk, R. W., & Sojka, J. J. (1996). Ionosphere–thermosphere space weather issues. *Journal of Atmospheric and Terrestrial Physics*, *58*(14), 1527–1574. https://doi.org/10.1016/0021-9169(96)00029-3

Thampi, S., Lin, C. H., Liu, H., & Yamamoto, M. (2009). First tomographic observations of the midlatitudes summer night anomaly (MSNA) over Japan. *Journal of Geophysical Research*, *114*, A10318. https://doi.org/10.1029/2009JA014439

Tulasi Ram, S., Rama Rao, P. V. S., Niranjan, K., Prasad, D. S. V. V. D., Sridharan, R., Devasia, C. V., & Ravindran, S. (2006). The role of post-sunset vertical drifts at the equator in predicting the onset of VHF scintillations during high and low sunspot activity years. *Annales de Geophysique*, *24*(6), 1609–1616. https://doi.org/10.5194/angeo-24-1609-2006

Uma, G., Brahmanandam, P. S., & Chu, Y. H. (2016). A long-term study on the deletion criterion of questionable electron density profiles caused by ionospheric irregularities - COSMIC radio occultation technique. *Advances in Space Research*, *57*(12), 2452–2463. https://doi.org/10.1016/j.asr.2016.03.034

Watthanasangmechai, K., Supnithi, P., Lerkvaranyu, S., Tsugawa, T., Nagatsuma, T., & Maruyama, T. (2012). TEC prediction with neural network for equatorial latitude station in Thailand. *Earth Planet Space*, *64*(6), 473–483. https://doi.org/10.5047/eps.2011.05.025

Widrow, B., & Hoff, M. E. (1960). *Adaptive Switching Circuits* (pp. 96–104). Institute of Radio Engineers (IRE) WESCON Convention record.

Widrow, B., & Lehr, M. A. (1993). Adaptive neural networks and their application. *International Journal of Intelligent Systems*, *8*(4), 453–507. https://doi.org/10.1002/int.4550080403

Williscroft, L.-A., & Poole, A. W. A. (1996). Neural networks, f_oF_2, sunspot number and magnetic activity. *Geophysical Research Letters*, *23*(24), 3659–3662. https://doi.org/10.1029/96GL03472

Wintoft, P. (2000). Twenty-four hour predictions of f_oF_2 using neural networks. *Radio Science*, *35*, 395–408.

Xenos, T. D. (2002). Neural-network-based prediction techniques for single station modelling and regional mapping of the f_oF_2M(3000)F_2 ionospheric characteristics. *Nonlinear Processes in Geophysics*, *9*(5/6), 477–486. https://doi.org/10.5194/npg-9-477-2002

Yang, K. F., Chu, Y. H., Su, C. L., Ko, H. T., & Wang, C. Y. (2009). An examination of FORMOSAT-3/COSMIC ionospheric electron density profile: Data quality criteria and comparisons with the IRI model. *Terrestrial, Atmospheric and Oceanic Sciences*, *20*(1), 193–206. https://doi.org/10.3319/TAO.2007.10.05.01%20(F3C)

Yonezawa, T. (1971). The solar-activity and latitudinal characteristics of the seasonal, non-seasonal and semi-annual variations in the peak electron densities of the F_2-layer at noon and at midnight in middle and low latitudes. *Journal of Atmospheric and Solar: Terrestrial Physics*, *33*, 887–907.

Yue, X., Schreiner, W. S., Pedatella, N., Anthes, R. A., Mannucci, A. J., Straus, P. R., & Liu, J. Y. (2014). Space weather observations by GNSS radio occultation: From FORMOSAT-3/COSMIC to FORMOSAT-7/COSMIC-2. *Space Weather*, *12*, 616–621. https://doi.org/10.1002/2014SW001133

Zeng, Z., Burns, A., Wang, W., Lei, J., Solomon, S., Syndergaard, S., … Kuo, Y.-H. (2008). Ionospheric annual asymmetry observed by the COSMIC radio occultation measurements and simulated by the TIEGCM. *Journal of Geophysical Research*, *113*, A07305. https://doi.org/10.1029/2007JA012897

Zhao, X., Ning, B., Liu, L., & Song, G. (2014). A prediction model of short-term ionospheric f_oF_2 based on AdaBoost. *Advances in Space Research*, *53*(3), 387–394. https://doi.org/10.1016/j.asr.2013.12.001

Zhelavskaya, I. S., Spasojevic, M., Shprits, Y. Y., & Kurth, W. S. (2016). Automated determination of electron density from electric field measurements on the Van Allen Probes spacecraft. *Journal of Geophysical Research: Space Physics*, *121*, 4611–4625. https://doi.org/10.1002/2015JA022132

Zhou, C., Wang, R., Lou, W., Liu, J., Ni, B., Deng, Z., & Zhao, Z. (2013). Preliminary investigation of real-time mapping of f_oF_2 in northern China based on oblique ionosonde data. *Journal of Geophysical Research: Space Physics*, *118*, 2536–2544. https://doi.org/10.1002/jgra.50262